

Electron Backscatter Diffraction Analysis of Inconel 718 Parts Fabricated by Selective Laser Melting Additive Manufacturing

XIAOQING WANG¹ and KEVIN CHOU^{1,2}

1.—Department of Mechanical Engineering, The University of Alabama, Tuscaloosa, AL 35487, USA. 2.—e-mail: kchou@eng.ua.edu

In this study, the crystallographic texture of an Inconel 718 part fabricated by selective laser melting was investigated. The front surface (X–Z plane) microstructure is characterized by the columnar grains growing along the build direction, and the width of columnar grains is in the range of about 75–150 μm , with the bottom layers having narrower grains as a result of a higher cooling rate. In addition to equiaxed grains, the top surface (X–Y plane) has a feature of patch patterns resulting from the laser scanning strategy. Based on the electron backscatter diffraction results, there appears only weak crystallographic texture in both the X–Z plane and the X–Y plane of the part. From the grain boundary map, the microstructures are composed of high-angle boundaries with a larger fraction of subgrain boundaries.

INTRODUCTION

Additive manufacturing (AM) is currently one of the most rapidly developing advanced manufacturing techniques in the world¹ and has exhibited extensive application.² It has presented various benefits, such as (I) improving the production development cycle, (II) allowing for making of complex-shaped parts, (III) saving cost by optimizing material usage, (IV) capable of fabricating functionally graded parts, and (V) allowing for fully customized parts to suit the individual.^{3,4} Among the AM technologies, the powder-bed laser technologies⁵ have shown critical applications for aerospace materials, such as titanium alloys and nickel-based alloys.^{6–8} Selective laser melting (SLM), which is capable of producing geometrically complex components with high dimensional precision and good surface integrity, has been recognized as a promising powder-bed, laser-based AM technology.⁹ In SLM, an inert argon or nitrogen gas is used as the atmospheric environment, along with a computer-controlled scanning laser beam, is applied as the energy source to melt the pre-spread powder particles selectively layer by layer.¹⁰

As a nickel-based alloy, Inconel 718 (IN718) has experienced extensive development over the past four decades¹¹ and has demonstrated outstanding mechanical properties and superior performances in the aerospace industry, such as gas turbines.¹²

Nevertheless, as a result of tool overwear and poor workpiece surface integrity, the high hardness and low thermal conductivity characteristics of IN718 make it very difficult to manufacture products using conventional machining methods, especially for those having complex structures. Experimental investigations regarding microstructures of SLM-processed IN718 components have been carried out. Wang et al.¹³ noted that regular laser-melted tracks with good metallurgical bonding, minimal defects, and fine dendritic grains can be formed by SLM. Amato et al.¹⁴ observed that the fabricated components exhibited a more pronounced columnar γ'' phase precipitate architecture parallel to the build direction (spaced at $\sim 0.8 \mu\text{m}$). Parimi et al.¹⁵ investigated the microstructural and texture development in direct laser fabricated IN718 alloy. Considerable differences were observed in that the high laser power input generated a columnar grain structure with a strong $\langle 001 \rangle$ fiber texture along the build direction, whereas the low-power builds showed a mixture of fine uniform and large columnar grains with a near random texture. In addition, the mechanical properties of SLM-processed IN718 also have been investigated. Wang et al.¹³ reported that the yield strength (YS), tensile strength (TS), and microhardness are 903 MPa, 1143 MPa, and 3.58 GPa (HV 365), respectively. The TS and microhardness obtained by Amato et al.¹⁴ are 1120 MPa and 3.9 GPa, respectively. In addition,

Cao et al.¹⁶ reported that the averaged hardness values at the fusion zone and the heat affect zone for the welded samples are 2.82 GPa (HV 287.6) and 2.39 GPa (HV 233.6), respectively.

Although various aspects in SLM-processed IN718 have been investigated,^{13,17–21} the microstructural and textural anisotropy on build surfaces and side surfaces are inevitably affected by process parameters, but they have yet to be studied.²² The microstructure and texture evolution may affect the mechanical properties and performances of SLM-built parts. In this study, an IN718 part was fabricated by SLM. The relationship among SLM microstructural characterization and texture evolution would be established.

EXPERIMENT

A concept laser M2 laser cusing system at the Marshall Space Flight Center (Huntsville, AL) of the National Aeronautics and Space Administration (NASA) was used to fabricate the solid block with a dimension of 40 mm by 40 mm by 6 mm at room temperature (25°C). The schematic of the system is illustrated in Fig. 1a. Fine pre-alloyed gas atomized powder was used as raw material, and an island pattern was used as the scan strategy with its schematic diagram shown in Fig. 1b.²⁴ For each island, simple alternating scan vectors with a speed of 600 mm/s were used with a scan spacing of 105 μm .

After the build, the part was stress relieved and sectioned off the stainless steel base plate. As shown in Fig. 1c, eight samples (S1–S8) were prepared with standard metallographic procedures to examine the anisotropic characterizations, in which S1–S4 were used to investigate the front surface (X–Z plane) and S5–S8 were used to study the top surface (X–Y plane). The X–Z plane was chosen as there is no expected difference in microstructures between the Y–Z and X–Z planes. Optical microscope (OM) and electron beam backscatter diffraction (EBSD) techniques were used to reveal the microstructure and crystallographic orientation information of the samples. To quantify the size of columnar γ , a measurement method, from Wang et al.,¹³ was applied.

MICROSTRUCTURES OF AS-FABRICATED IN718

Typical Structures on X–Z Plane and X–Y Plane

The X–Z plane presents a unidirectional columnar structure along the Z-direction, perpendicular to the melted powder layers caused by the vertical heat flux related to heat transfer into the substrate, as shown in Fig. 1d, e, and f. Extensively grown grains across several deposit layers can also be observed occasionally. As the process of SLM is based on the condition of complete melting and solidification, the columnar γ dendrite architecture was formed by means of the heterogeneous

nucleation of γ nuclei and subsequent dendrite growth during the manufacturing process. Upon rapid cooling from the melt, the growing grains aligned themselves with the steepest temperature gradients and result in columnar shaped morphology.²⁵

As shown in Fig. 1g, the X–Y plane is characterized by equiaxed grains, which results from epitaxial, dendritic grain growth in the direction of heat flux and crystallographic alloy favored orientation.²⁶ The horizontal heat flux is related to the movement of the heat source. The grains would be in a rod-shape if considering the observation in a X–Z plane and X–Y plane together, which has also been observed by Amato et al.¹⁴ and Gong et al.²¹

Columnar Width Diversity Along Built Height

Generally, the average width of the columnar structures increases with the building height of the part, as shown in Supplemental Table I. As shown in Fig. 1f, the bottom layers present narrow and uniformly distributed columnar dendrites. The first few melt layers are in direct contact with the stainless steel substrate plate, which has a lower temperature (about 300°C) and a much higher thermal conductivity compared with the melt pool of IN718. This results in a larger cooling rate for the bottom layers. An increase in the cooling rate will form smaller columnar grains²⁷ because more nuclei could be generated at a higher cooling rate. This will further form finer grains in long and narrow columnar morphology ($\sim 75 \mu\text{m}$). With an increase in build height, the cooling rate will decrease and then the width of the columnar structure on the X–Z plane will increase until it achieves an equilibrium situation where the size ($146.77 \pm 11.04 \mu\text{m}$) is around the diameter of the spot size (150 μm). This leads to a uniformly columnar structure, as can be seen in Fig. 1e.

The S1 and S3 have a larger standard deviation for their width of the columnar structures, which results from transition of the microstructure caused by the changing of the cooling rates. As shown in Fig. 1d, S1 shows a clear transition of the microstructure with its width changing from $\sim 147 \mu\text{m}$ to $\sim 75 \mu\text{m}$. The top layers present a very fine microstructure as they are in contact with the environment temperature in the chamber, which leads to a higher cooling rate compared with that in the middle of the part.

TEXTURE ANALYSIS IN SLM

The orientation maps from the X–Z plane (S1–S4) are shown in Fig. 2a, b, c, and d. The grain features of laser melting are shown clearly, such as the configuration of the grains and columnar architecture throughout the X–Z plane. This geometry was determined by the specimen building strategy, such as the laser scanning pattern, hatch spacing, and thickness of layers. The cut ends of the grains in the form of a series of arcs on the X–Z plane are induced by the

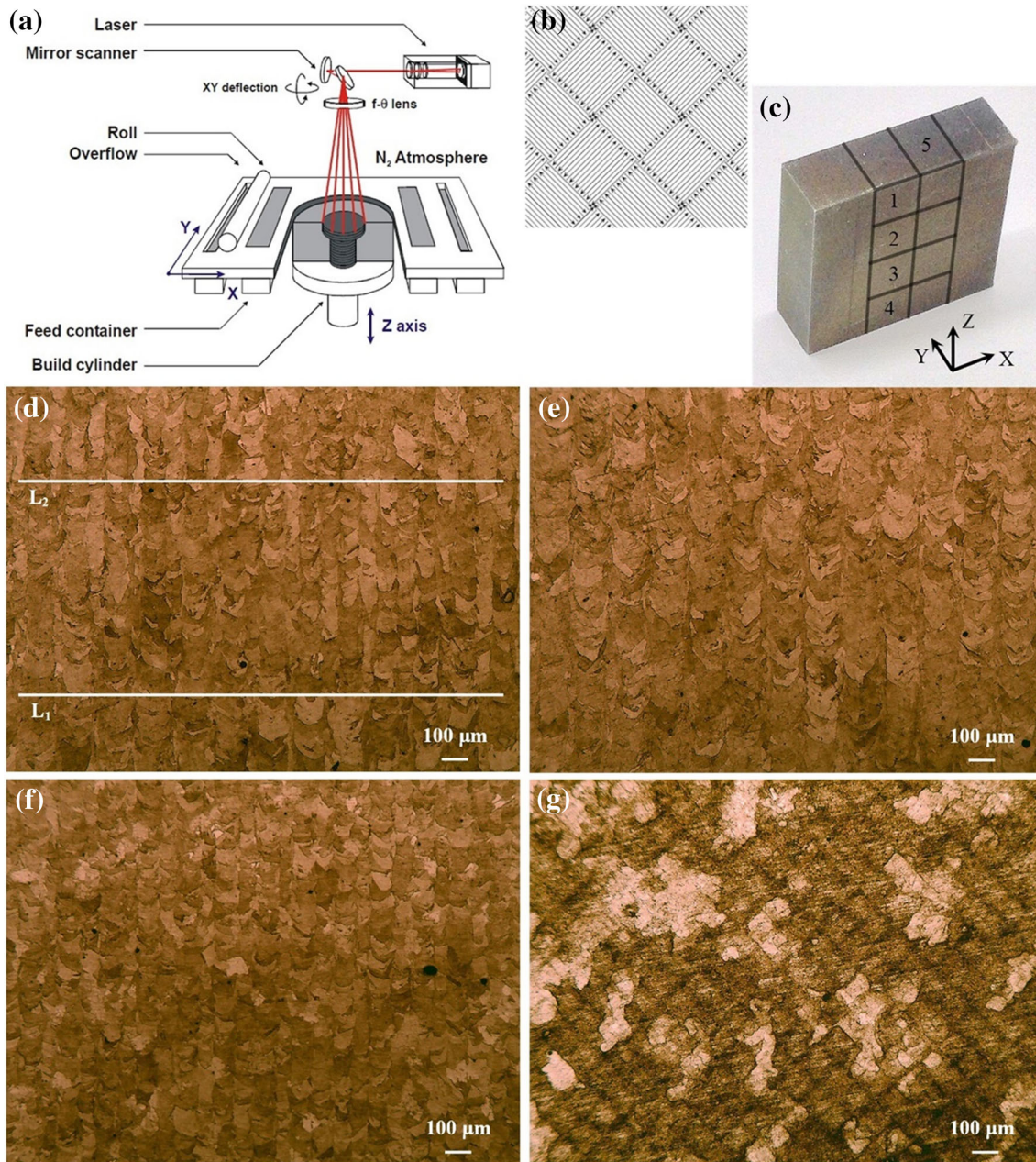


Fig. 1. Schematic of (a) a SLM machine²³ and (b) the island scan strategy, (c) as-processed part, and microstructure on X-Z plane (d) S1, (e) S2, (f) S4, and X-Y plane (g) S8.

Gauss energy distribution of laser in the melt pool.¹³ At the intersection of the columnar structures, there are a lot of elongated grains growing through several layers, which would be caused by the remelting process as a result of the overlap of the scanning lines resulting from the smaller scanning space ($105\ \mu\text{m}$) compared with the beam spot size ($150\ \mu\text{m}$).

The pole figures corresponding to the orientation maps are shown in Fig. 2e, f, g, and h. Generally, the degree of the prominent orientation decreased from the top to the bottom of the samples. The existence of a fiber texture in samples is because the grain dendrites are oriented parallel to the heat flow

direction. The main heat transfer path is from the melt pool to the substrate plate, which has a maximum temperature gradient at the Z-direction. Solidification occurs by the formation of nuclei and/or growth of crystals, and either of them may be predominant depending on the solidification conditions. As shown in the orientation maps, the growth of the columnar-grain texture has been interrupted by grains of random orientation formed at the solidification front. This suggests that nucleation of new grains is more effective in accommodating the undercooling at the solidification front than is the growth and branching of the dendrites in the

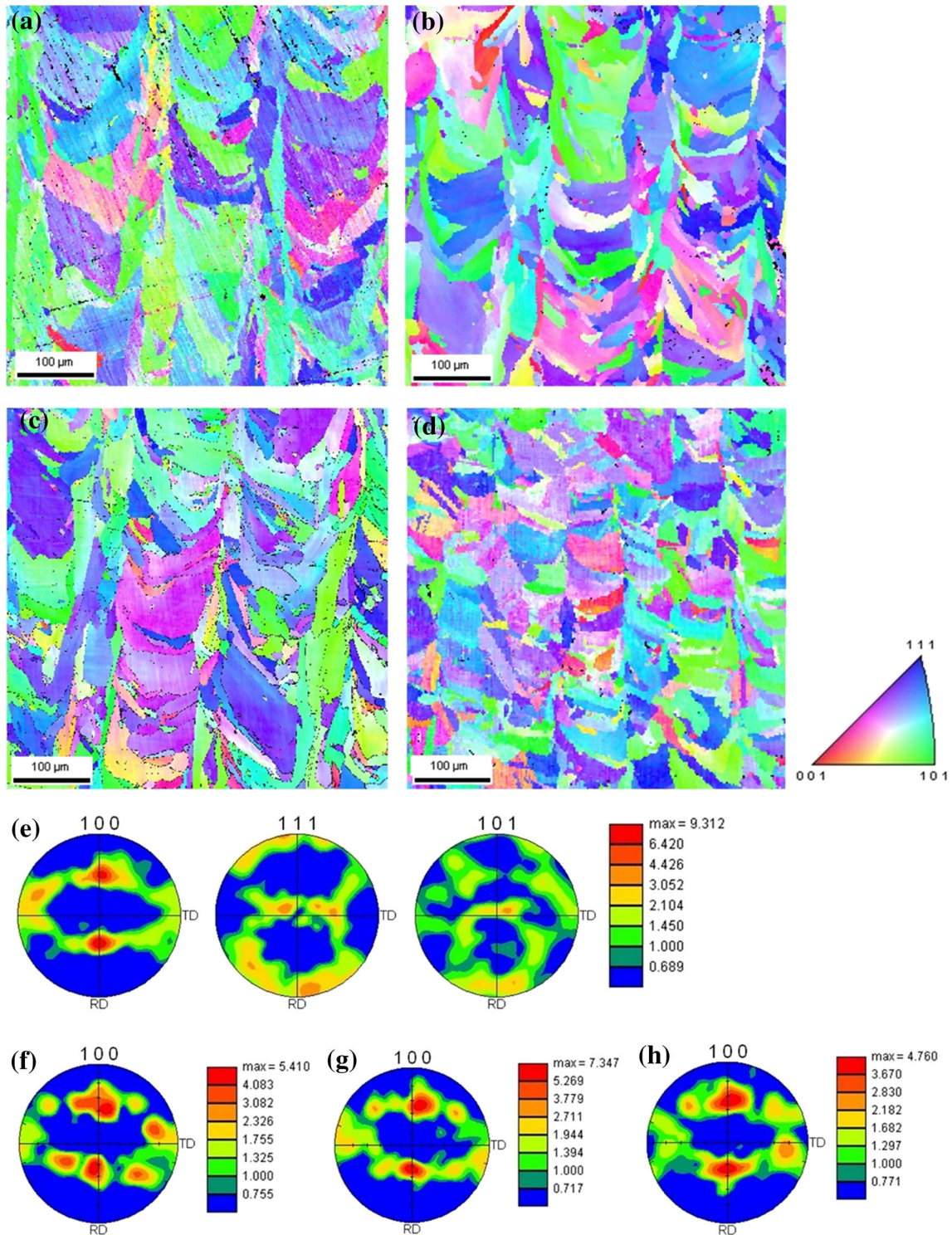


Fig. 2. (a–d) are orientation maps from S1, S2, S3, and S4, respectively, and (e–h) are pole figures corresponding to (a–d), sequentially.

existing columnar grains. The fastest growth direction of the base γ phase is the $\langle 1\ 0\ 0 \rangle$ direction. Thus, the grains generally grew in the Z-direction with the orientation of $\langle 1\ 0\ 0 \rangle$ along with the build of the part. The S4 has the weakest texture because the first melt layers were in direct contact with the

substrate stage, which led to a larger cooling rate without a particular direction. So more nuclei were formed and most of them grew in the random way. After that, the nucleation of new grains occurred in some region at the solid–liquid interface between the melt pool and the former layers. The grains,

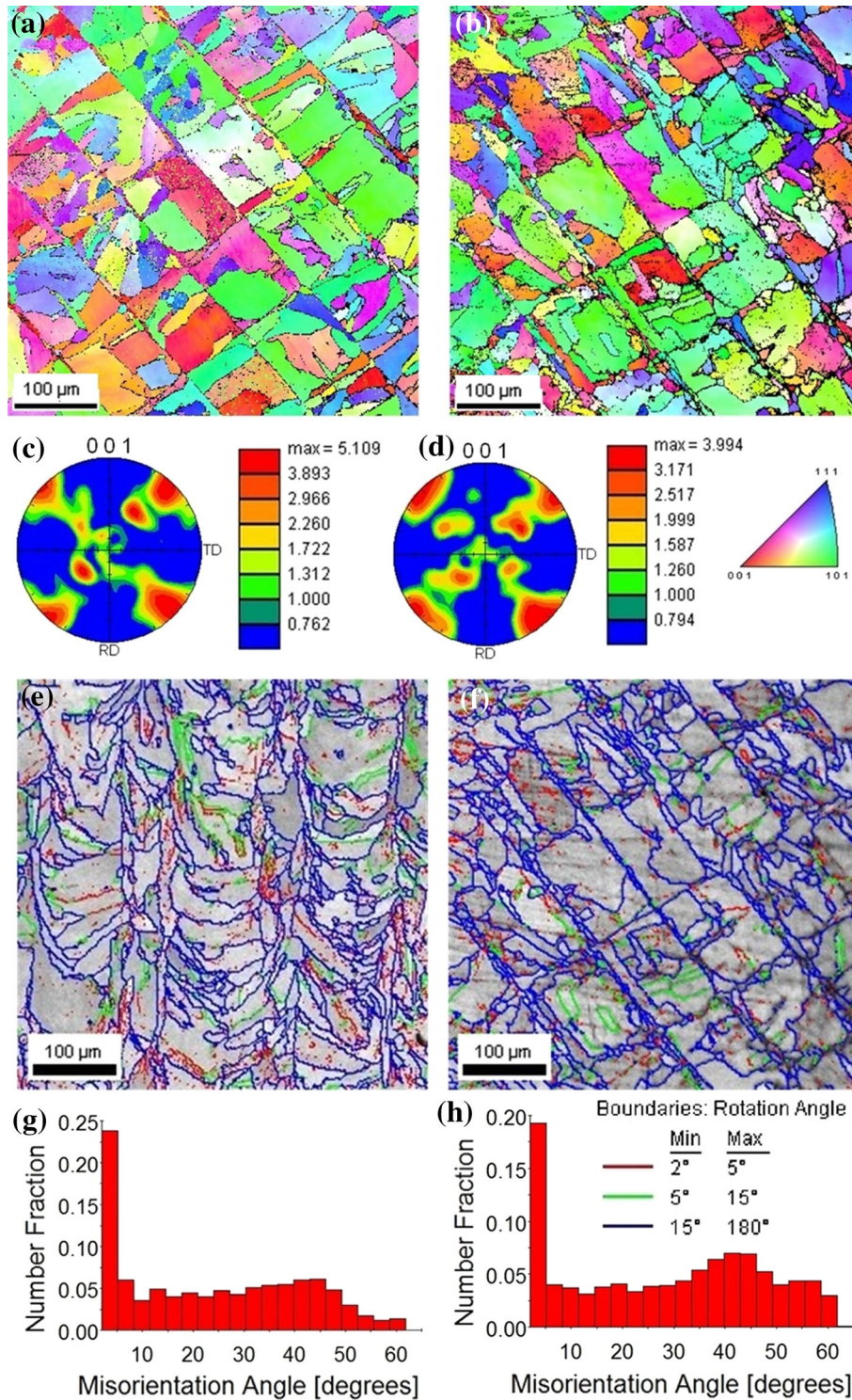


Fig. 3. (a, b) are orientation maps from X-Y plane of S5 and S8, respectively, (c, d) are pole figures corresponding to (a, b), (e, f) are the typical misorientation angle map from X-Z plane (S2) and X-Y plane (S8), and (g, h) are the statistics results corresponding to (e, f).

having a $\langle 100 \rangle$ direction nearly parallel to the heat flow direction, grew rapidly, whereas the growth of other grains ceased. Therefore, columnar grains formed with most of them having a $\langle 100 \rangle$

crystallographic orientation. As mentioned, the top layers have a higher cooling rate, which leads to a slightly strong grain orientation, as shown in Fig. 2e.

The orientation maps of the X–Y plane from the top and bottom samples are shown in Fig. 3a and b. The scanning pattern with a width around 100 μm is shown, and there are numerous small-sized grains at the interface of the scanning paths. During the manufacturing process, the main heat transfer way on the top surface was from the inside to the boundary of the layers. This led to a fast growth for some grains with the $\langle 1\ 0\ 0 \rangle$ orientation parallel to the heat flow direction. Then, solidification occurred by the epitaxial growth of crystal from the melt pool. The pole figures from the X–Y plane reveal a weak edge-on-cube texture component presenting in the as-deposit IN718 sample, as shown in Fig. 3c and d. This is a common texture in face-centered cubic metals subjected to static recrystallization. This texture results in the anisotropy in the as-deposited samples, which also has been mentioned by Tayon et al.²⁸ Compared with the X–Z plane, the X–Y plane was generally found to have a weaker texture, although the overall texture of the entire build seemed to be a complex composite cluster of textures.

Figure 3e and f presents the typical grain boundary maps, in which different colors represent different boundary rotation angles. The statistics results are shown in Fig. 3g and h. The majority boundary angles are above 15° , which are called high-angle grain boundaries. This will lead to the instability of the microstructure because the high energy accumulated in the form of grain boundaries and, to a lesser degree, of dislocations. To obtain the microstructure composing of a stable γ phase strengthened with coherent and dispersive precipitates of the phases, γ' and γ'' , post heat treatment is needed.¹⁷ The presence of high-angle grain boundaries also could strongly affect both the density and the distribution of the cracks in the as-fabricated material.²⁴ The as-deposited material is more susceptible to ductility dip cracking at high-angle grain boundaries.

There is some evidence of micro-segregations within the grains or at the grain boundaries, as shown clearly in Fig. 3a and b. During solidification, dendrites formed and this would cause Nb and other alloy elements to segregate at the interdendritic regions.²⁹ This leads to the formation of the Laves phase, which are irregularly shaped phases with a typical composition of $(\text{Ni}, \text{Fe}, \text{Cr})_2(\text{Mo}, \text{Nb}, \text{Ti})$. They are detrimental to mechanical properties and can be dissolved in the matrix by proper heat treatments.⁶ Thus, the as-fabricated builds have to be improved by performing heat treatment as they generally have poor mechanical properties as a result of these defects.

CONCLUSION

IN718 parts were fabricated using an SLM machine with default process parameters. Eight samples were prepared for microstructure and

texture analysis. The results show that the X–Z plane specimens exhibit columnar microstructures with an average width of 75–150 μm . The columnar grains at the bottom layers appear narrower possibly because of a higher cooling rate. The X–Y plane specimens show equiaxed grains with a feature of patch patterns (each about 100 μm by 100 μm) resulting from the scanning strategy. Based on the EBSD results, there appears only a weak crystallographic texture in both the X–Z plane and X–Y plane surfaces of the parts. Moreover, from the grain boundary map, the microstructures are composed of high-angle boundaries with a larger fraction of subgrain boundaries, which may result in the instability of the microstructures and require heat treatments after the SLM process.

ACKNOWLEDGEMENTS

This research is partially supported by CFD Research Corporation (Huntsville, AL) through a NASA STTR project. The Marshall Space Flight Center (Huntsville, AL) fabricated experimental samples. XW also acknowledges scholarship support from the Alabama EPSCoR GRSP. Dr. Xibing Gong (The University of Alabama) initiated preliminary analysis.

ELECTRONIC SUPPLEMENTARY MATERIAL

The online version of this article (doi:[10.1007/s11837-016-2198-1](https://doi.org/10.1007/s11837-016-2198-1)) contains supplementary material, which is available to authorized users.

REFERENCES

1. D. Gu, W. Meiners, Y.-C. Hagedorn, K. Wissenbach, and R. Poprawe, *J. Phys. D Appl. Phys.* 43, 295402 (2010).
2. I. Gibson, D.W. Rosen, and B. Stucker, *Additive Manufacturing Technologies*, 2nd ed. (New York: Springer, 2010), pp. 138–140.
3. D. Gu, *Laser Additive Manufacturing of High-Performance Materials*, 2nd ed. (Berlin: Springer, 2015), pp. 6–7.
4. K. Shah, A. Khan, S.A. Shah, M. Khan, and A.J. Pinkerton, *Mater. Des.* 54, 531 (2014).
5. K. Osakada and M. Shiomi, *Int. J. Mach. Tools Manuf* 46, 1188 (2006).
6. C.H. Radhakrishna and K.P. Rao, *J. Mater. Sci.* 32, 1977 (1997).
7. J. Ma, F. Kong, W. Liu, B. Carlson, and R. Kovacevic, *J. Mater. Process. Technol.* 214, 1696 (2014).
8. X. Wang, X. Gong, and K. Chou, *Mech. Eng. B J. Eng.* (2016). doi:[10.1177/0954405415619883](https://doi.org/10.1177/0954405415619883).
9. B. Vrancken, L. Thijs, J.-P. Kruth, and J. Van Humbeeck, *J. Alloys Compd.* 541, 177 (2012).
10. B. Zhang, H. Liao, and C. Coddet, *Vacuum* 95, 25 (2013).
11. L. González-Fernández, L. del Campo, R.B. Pérez-Sáez, and M.J. Tello, *J. Alloys Compd.* 513, 101 (2012).
12. C.M. Kuo, Y.T. Yang, H.Y. Bor, C.N. Wei, and C.C. Tai, *Mater. Sci. Eng., A* 510, 289 (2009).
13. Z. Wang, K. Guan, M. Gao, X. Li, X. Chen, and X. Zeng, *J. Alloys Compd.* 513, 518 (2012).
14. K. Amato, S. Gaytan, L. Murr, E. Martinez, P. Shindo, J. Hernandez, S. Collins, and F. Medina, *Acta Mater.* 60, 2229 (2012).

15. L.L. Parimi, D. Clark, and M.M. Attallah, *Mater. Charact.* 89, 102 (2014).
16. X. Cao, B. Rivaux, M. Jahazi, J. Cuddy, and A. Birur, *J. Mater. Sci.* 44, 4557 (2009).
17. E. Chlebus, K. Gruber, B. Kuźnicka, J. Kurzac, and T. Kurzynowski, *Mater. Sci. Eng., A* 639, 647 (2015).
18. Q. Jia and D. Gu, *J. Alloys Compd.* 585, 713 (2014).
19. X. Wang and K. Chou, in *Solid Freeform Fabrication Symposium Proceedings* (2015), p. 1463.
20. X. Wang and K. Chou, in *Proceedings of ASME's International Mechanical Engineering Congress and Exposition* (ASME, 2015), p. V02AT02A002.
21. X. Gong, X. Wang, V. Cole, Z. Jones, K. Cooper, and K. Chou, in *Proceedings of ASME's International Mechanical Engineering Congress and Exposition* (ASME, 2015), p. V001T02A061.
22. L. Thijs, F. Verhaeghe, T. Craeghs, J.V. Humbeeck, and J.-P. Kruth, *Acta Mater.* 58, 3303 (2010).
23. J.-P. Kruth, P. Mercelis, J. Van Vaerenbergh, L. Froyen, and M. Rombouts, *Rapid Prototyp. J.* 11, 26 (2005).
24. L.N. Carter, C. Martin, P.J. Withers, and M.M. Attallah, *J. Alloys Compd.* 615, 338 (2014).
25. X. Wang, X. Gong, and K. Chou, *Proc. Manuf.* 1, 287 (2015).
26. M. Ardakani, N. D'Souza, A. Wagner, B. Shollock, and M. McLean, *Superalloys* (TMS, 2000), p. 219.
27. J. Gockel and J. Beuth, in *Solid Freeform Fabrication Symposium Proceedings*, Austin, TX, Aug, 12 (2013).
28. W.A. Tayon, R.N. Shenoy, M.R. Redding, R.K. Bird, and R.A. Hafley, *J. Manuf. Sci. Eng.* 136, 061005 (2014).
29. W.J. Sames, K.A. Unocic, R.R. Dehoff, T. Lolla, and S.S. Babu, *J. Mater. Res.* 29, 1920 (2014).